EXPERIMENTAL AND NUMERICAL SIMULATIONS OF NACA 0018 AIRFOIL UNDERGOING STALL FLUTTER WITH STRUCTURAL NONLINEARITY

Muhamad K. H. M. Zorkipli[1], Ahmad F. Razaami[1], and Norizham A. Razak [1]

[1] School of Aerospace Engineering
Universiti Sains Malaysia
Engineering Campus, Nibong Tebal
Penang, Malaysia
norizham@usm.my

Keywords: Stall flutter, nonlinearity, wind tunnel test, numerical simulation.

Abstract: The aeroelastic behaviour of a wing oscillating in large pitch amplitudes with continuos nonlinear stiffness is examined by means of wind tunnel experiments and numerical simulations. The phenomena of interest is limit cycle oscillation resulted from stall flutter. The focus of the present work is the dynamic behaviour of aeroelastic system consisting of aerodynamic nonlinearity, prescribe and unprescribe structural nonlinearity. Unprescribe structural nonlinearity manifested through changes in stiffness property during limit cycle oscillation due to fatigue. The interaction of flow separation nonlinearity with structural nonlinearities is examined. The measured and simulated aeroelastic responses are analyzed and the bifurcation behavior of the dynamic system is characterized. The analysis shows that the bifurcation behaviour is dictated structural nor from the aerodynamic nonlinearity but by a combination of the two.

1 INTRODUCTION

Dynamic aeroelastic phenomena are the phenomena resulting from the mutual interaction of aerodynamic forces, inertia forces and elastic forces of flexible structures. Classical flutter and other phenomena such as buffeting and galloping fall under this category, for example the classical bending-torsion flutter is a self-excited oscillation that leads disastrous consequences.

Another phenomenon can arise from aeroelastic effects is stall flutter. Stall flutter is a phenomenon that occurs when the flow separates from and reattaches from any aerodynamic surface in a repeating manner. Complete or partial separation of flow over the entire upper wing surface has been observed during stall flutter oscillation. The behavior involves an alternation between stalled and attached flow over wings. Halfman et al [1] and Rainey [2] characterized stall flutter as a motion that involves primarily torsional vibrations; there is a severe drop in the critical flutter speed and the flutter frequency approaches the pitching frequency.

Stall flutter has been encountered in blades of rotary wing aircraft [3] and wind turbine operating at high angle of attack [4]. Flow visualizations performed on the flow field around a wing undergoing stall flutter oscillations revealed free vortices often generated in the vicinity of the flow separation points [5]. Stall flutter is also associated with the

existence of nonlinearity in the aerodynamic forces; the phenomenon may occur in a single degree of freedom and the amplitude of oscillation will often be limited by the aerodynamic nonlinearities [6]. The vortex generation in many cases indicates the existence of dynamic stall phenomenon. Dynamic stall is the significant and abrupt loss of aerodynamic loads (lift and pitching moment) due to flow separation on wings undergoing unsteady motion.

Extensive work regarding stall flutter and oscillating wings was performed by McAlister *et al* [7] with the objectives of creating a database for the NACA 0012 airfoil. This work was later extended to include other wings shapes and a wider range of parameters. The experiments showed that the unsteady motion parameters play a crucial role in determining the unsteady aerodynamic loads generated [8]. Stall flutter with structural freeplay was studied by Dimitriadis and Li [4]. They observed symmetrical and unsymmetrical bifurcation partly contributed by dynamic stall phenomenon. Razak and colleagues [9] examined the effect of airspeed and initial angle of attack on stall flutter behavior. Their results revealed 2 levels of LCO amplitudes correspond to partial or complete separation around the wing. Partial separation manifest from the trailing edge, while large amplitude LCO was caused by separation from leading edge.

Many experimental studies of the purely aerodynamic phenomenon of dynamic stall have been performed in the past; the aeroelastic phenomenon of stall flutter has still not been thoroughly investigated. Recent work [4, 9] has shown that the stall flutter bifurcation behavior is very complex, including subcritical Hopf, folds and symmetry-breaking bifurcations. The existence of structural nonlinearity would diversified the bifurcation behavior of stall flutter.

Apart from experimental works, numerical simulation has been used to study the dynamic behaviour of aeroelastic system with structural and aerodynamic nonlinearities. A fluid structure interaction (FSI) method is widely used in computational fluid dynamic software to study the aeroelastic system. A computational aeroelastic simulations of self-sustained pitch oscillations of NACA0012 at transitional Reynold numbers were performed by Poirel and colleagues [10] to validate with wind tunnel observation results. They employed a commercial CFD solver to simulate the aeroelastic system by using experimental parameters. RANS (SST) k-ω model with a low-Reynolds number correction option were used. The results obtained showed a reasonably accurate limit cycle pitching amplitudes and LCOs frequencies within a range observed in the experimental. From the numerical observation, laminar boundary separation layer caused the oscillation to kick in as observed in the wind tunnel. Yuan [11] performed a two degree of freedom self-sustained oscillation at low Reynolds number which is the extension from single degree of freedom performed by Poirel *et al* [10]. The simulations were carried out by using Large eddy simulation (LES) method to study the 2 DOF aeroelastic system. LES based calculation was able to capture the laminar separation bubble (LSB) and produced LCOs results for both heaving and pitching motion. The simulation results confirmed the Reynolds number affecting the LCO amplitudes and frequencies as in the experimental results.

In this work, the objective is to evaluate the dynamic behaviour of stall flutter with nonlinear structural stiffness. Different levels of structural nonlinearity were prescribed at various static attack angles. The investigation covers experimental and limited numerical simulation work.

2 EXPERIMENTAL SETUP

The experimental work was conducted in the Close Loop Wind Tunnel of the Universiti Sains Malaysia. The work involved the development, fabrication and testing of a single degree of freedom aeroelastic setup with prescribed nonlinear stiffness.

2.1 Aeroelastic Setup

In this work, Custom Aeroelastic Apparatus Setup (CAAS) was designed and constructed as shown in figure 2.1. The CAAS allows oscillations in heave and pitch degrees of freedom; the heaving motion is handled by a linear carriage traversing on two smooth linear bars but was constrained in this work. The pitch degree of freedom was obtained from attaching one end of an aluminum rod to the center of the linear carriage coupled to the nonlinear cam. The other end was connected to the NACA 0018 wing. The pitch angle sensor was attached to the wing spar via a pitch gear. The support mechanism described was designed to allow low friction oscillation with prescribed nonlinear structural stiffness values. The nature of the nonlinearity depends on the shape of the cam. The cam was designed to prescribe a mild cubic type nonlinear restoring force on the pitch degree of freedom at high pitch amplitude.

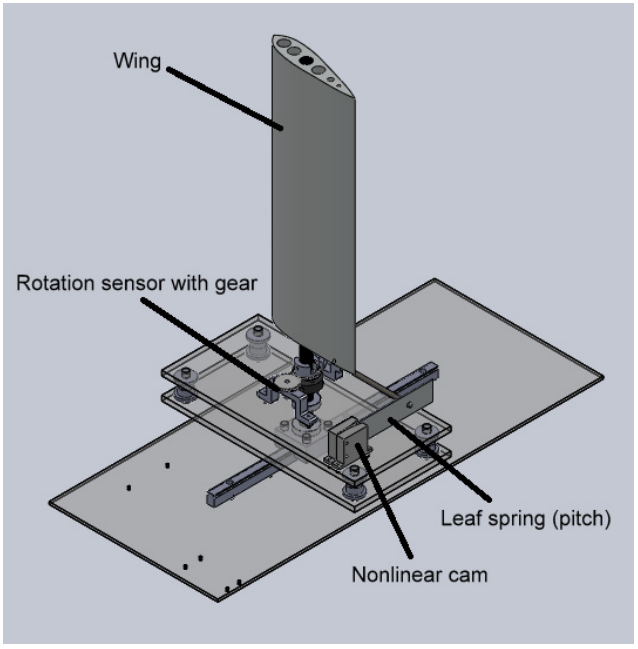

Figure 2.1: CAD drawing for wind tunnel test setup with nonlinear pitch stiffness.

The stiffness nonlinearity was achieved through nonlinear cam attached to the leaf spring that was connected to the airfoil's pitch mechanism. The cam was tailored to prescribed continuous nonlinearity in pitch degree of freedom. The three level of nonlinear stiffness (soft, medium and hard) were tested as shown in Figure 2.2. The leaf springs were made from aluminum plate measuring 0.2m x 0.04m with thickness of 0.05 cm. Anchoring the plate at different length varied the level of stiffness. For this study, there are three plates tested classified as A1, A2, A3 representing soft medium and hard cases.

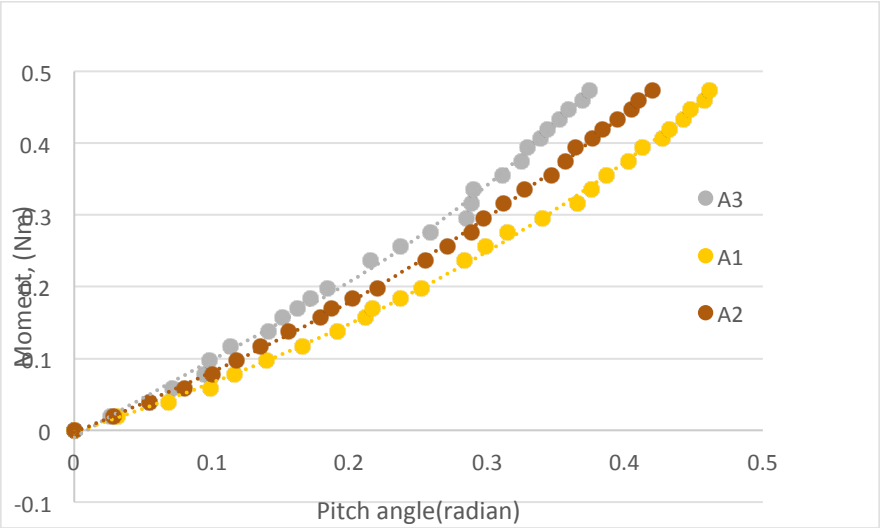

Figure 2.2: Restoring moment vs. pitch angle for three different cases

2.2 Wing

The rigid straight rectangular wing was made from aluminum. The skin was made from 0.05 cm aluminum sheet that wrapped around the balsa ribs. There were five ribs inside the wing, positioned 12.0 cm apart. The ribs, with thickness of 2 cm, were held together by a carbon fiber rod acting as a spar, located at the 40% of the chord. The profile selected for this study was a NACA 0018. The wing had a chord of 20.0 cm and the span is 49.5 cm. For this work, the mass of the wing including pitching mechanism was 1.16 kg. The wing was instrumented with 16 pressure taps connected to the pressure transducers via silicon tubes for capturing the unsteady static pressure distribution around the wing at mid span. The responses are measured using rotation sensor for further analysis.

2.3 Test Description

The experiments were divided into two phases. The first phase involves determining the natural frequencies of the system in pitch degree of freedom at wind-off conditions using impulse testing for all cases. The system was excited by applying impulses independent of the pitching degree of freedom. The impulses were applied on the leading and trailing edge to induce mainly pitching motion. Several impulses were applied to different points on the wing and the sensor responses were recorded and processed. The stiffness values shown in Table 1 were obtained by performing curve fit on the measured data. Other significant parameters such as mass moment of inertia, elastic axis and stiffness were also measured in this phase.

Case	Pitch Stiffness
A1	$0.8974x^3+0.3846x^2+0.6456x-0.0031$
A2	$1.1706x^3+0.3199x^2+0.7975x-0.0029$
A3	$4.7065x^3-1.1795x^2+1.1606x-0.0104$

Table 1: Stiffness for three different leaf springs

The second phase of testing involved measurements of the responses at wind-on condition. This series of tests were used to determine the critical airspeeds, amplitudes and the

frequencies of LCOs. The tests were conducted at various airspeeds at different pitch stiffness values. The wind-off angles of attack are set at 10°, 12°, 14°, 16°, 18° and 20°. It represents the static equilibrium position of the wing prior to being exposed to the airflow. The airspeed was varied between 0 m/s and 18 m/s. At each set of test parameters (airspeed and stiffness), the system was excited by applying an impulse in pitch mode and the responses were recorded. The recorded time depended on the type of the response encountered. Decaying responses only allowed short recording time while LCO responses were recorded for as long as 30 seconds. Once LCO was achieved, no more excitation was applied for higher airspeed cases. The system was allowed to oscillate until certain airspeed was reached where the amplitude was deemed too high to continue. Then the airspeed was reduced gradually until decaying oscillations were reached.

3 EXPERIMENTAL RESULTS

In this section, the characteristics of the wing's responses and their evolution with airspeed and stiffness are presented and discussed.

3.1 Responses

Figure 3.1 plots the two typical responses observed for case A1 at 12° of static angle of attack. The first type was decaying response. An initial impulse is applied to excite the structure and set it in motion; the amplitude of the resulting oscillations decays with time and the motion stops eventually. This behavior indicates loss of energy due to damping. The resulting response is shown in Figure 3.1(a), measured at 4.6 m/s that were prior to the onset airspeed. At lower airspeed (less than 4.6 m/s), the same effect was observed but with an increased rate of decay. This was caused from lower energy supplied by the airflow, which decreases but does not negate the structural damping.

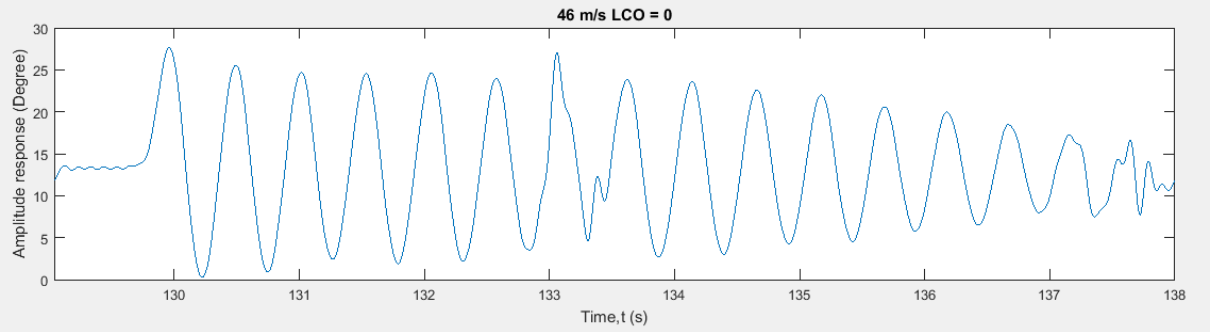

(a)

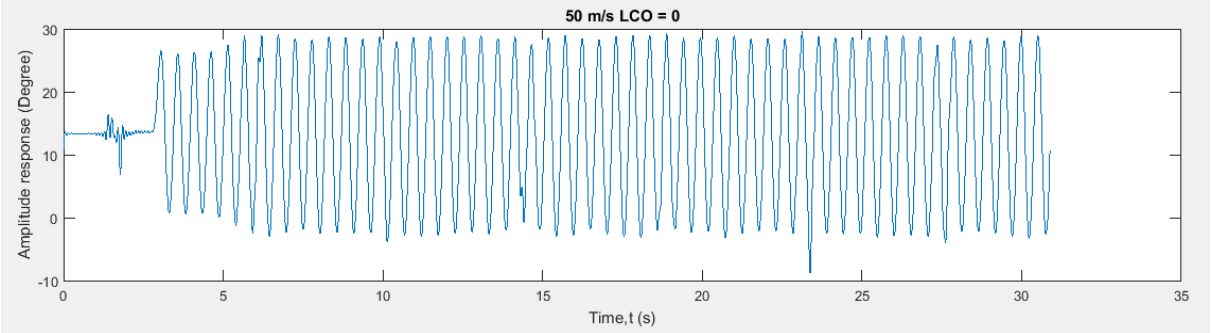

(b)

Figure 3.1: Pitch responses for plate A1 at 12° (a) at v = 4.6 m/s, (b) v = 5.0 m/s.

The second type of oscillation observed was the self-sustained limited amplitude oscillation shown in Figure 3.1(b) representing response measured at 5.0 m/s. After the initial perturbation, the system quickly settled to constant amplitude of oscillation. Increasing the airspeed resulted in a slight increase in amplitude. It should be noted that due to presence of bearing in the system, Coulomb damping is observed in the response.

The overall dynamic behavior observed for other cases exhibited the same two types of response. In addition, the LCO amplitude was also found to be sensitive to the level of the excitation impulse applied to the system. Results from case A1 showed the system exhibit LCOs at lower airspeeds than for other cases.

3.2 Frequency Content

Frequency analysis was performed on all measured responses in order to determine if there are any changes occurring with airspeed and pitch stiffness cases. Figure 3.2 shows the frequency content of the pitch responses measured for case A1 and A2 at various airspeeds tested. It shows the evolution of the frequency content at sub and post-critical conditions. Red lines represent increasing airspeeds starting form 0 m/s until certain airspeed was reached where the amplitude was deemed too high to continue. The airspeed was then decreased until the oscillation decayed. Blue lines represent the frequency content where the airspeed was reduced gradually until decaying response was reached.

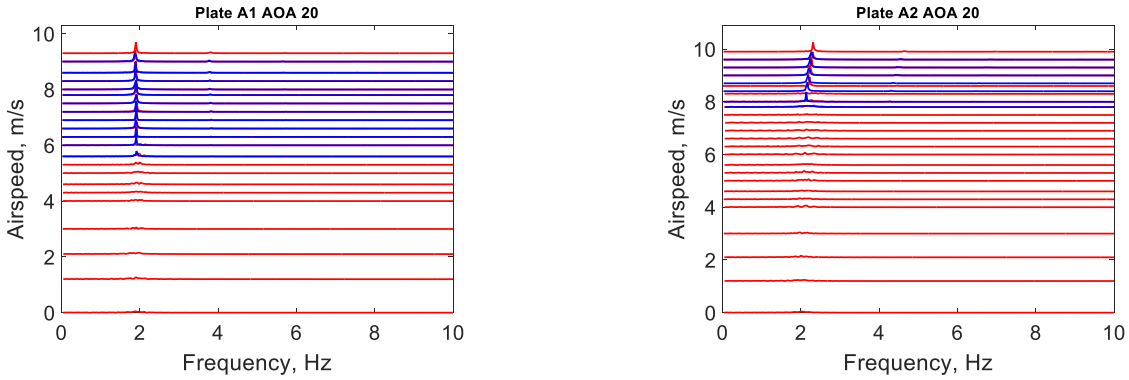

(a) (b)

Figure 3.2 : Frequency content for (a) case A1 at 20°, (b) case A2 at 20°.

From Figure 3.2(a), there is only small variation in oscillation frequency with increasing and decreasing airspeed. It can be said that a single frequency of 1.8Hz was observed at airspeed higher than 5.6 m/s. However as the stiffness was increased (for case A2), the oscillation frequency changed as the airspeed increased as shown in Figure 4(b). The LCO appeared at 8.6 m/s with a frequency of 2.1Hz. At maximum airspeed tested which was at 9.9 m/s, the frequency increased to 2.4Hz. The hardening effect was due to the continuous nonlinear stiffness prescribed via the nonlinear cam. Plate A3 also revealed the same hardening effect where the maximum frequency achieved was

3.3 Bifurcation Plot

Figure 3.3 shows the bifurcation plot of NACA 0018 undergoing stall flutter oscillation plotted for different static angles of attack for case A3. Black squares represent the maximum and minimum amplitude variations when the airspeed was increased from zero up to the

maximum airspeed tested. Blue circles represent the maximum and minimum amplitudes when the airspeed was reduced until decay oscillation were reached. The angles of attack cases shown in the figure are 10°, 12°, 14°, 16°, 18° and 20°. The bifurcation plot is presented in terms of the maximum and minimum values of oscillating amplitude, where the time derivative of the displacement response in equal to zero. The amplitudes plotted are the oscillation amplitude with respect to the static angle of attack. For airspeeds values for which no LCOs where observed the amplitudes were plotted as it's static angle of attack. For α_0 = 10°, it can be seen that the first LCO responses were obtained at U = 5.6 m/s with amplitude of ± 8.9°. Increasing the airspeed to 9.0 m/s led to jump of amplitude to ± 26.6° from equilibrium. This is the maximum airspeed tested for this case since the vibration amplitude was very high. It was decided not to increase the airspeed any further for safety reasons. Increasing and decreasing airspeed caused gradual changed in the pitch amplitude.

An increase of 2° in the static angle of attack brought out a significant change in the bifurcation condition. The critical airspeed was lower but, the post-critical behavior totally different. After the initial jump in pitch amplitude, it increased gradually as airspeed was increased. Data from the α_0 = 14° to 16° configuration show that the onset airspeeds were maintained. The onset airspeed decrease slightly at α_0 = 18° but jumped to 6.9 for α_0 = 20°. The maximum amplitude measured was + 48.5°.

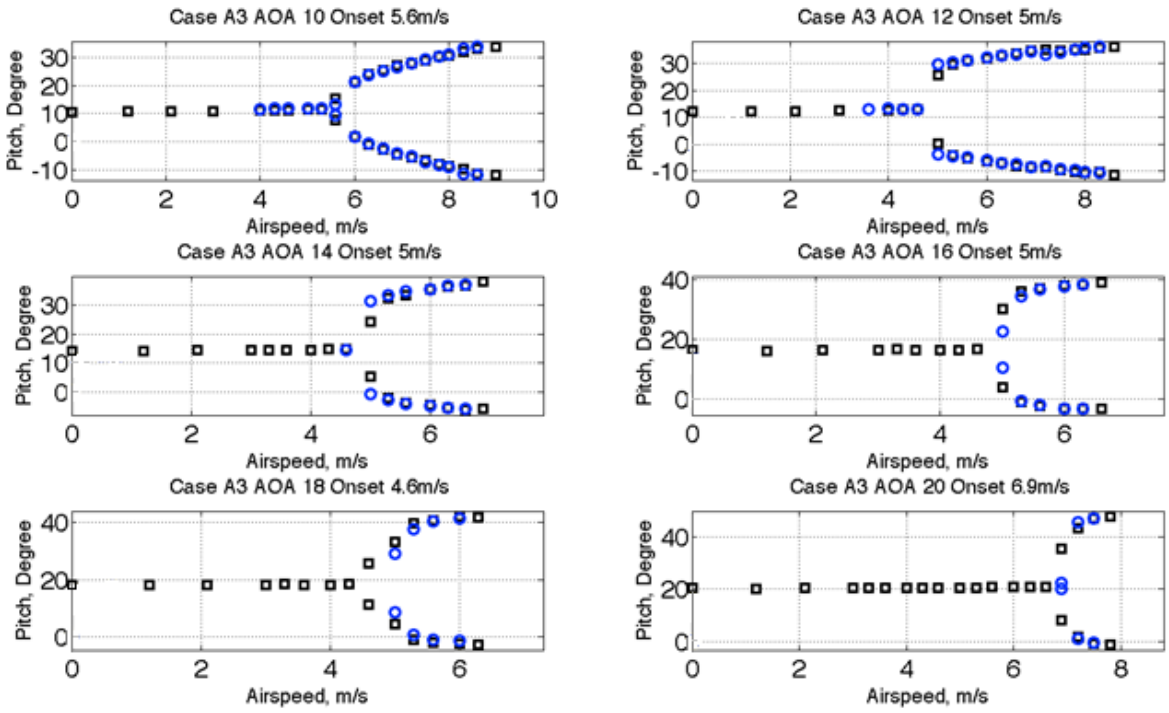

Figure 3.3 : Bifurcation plot for plate A3.

At α_0 = 20°, the response is steady until at a critical flight condition, it suddenly becomes oscillatory with enormous amplitude ± 28.7° from amplitude ± 25.2° where the measured LCO onset airspeed was 6.9 m/s. All oscillations measured in this research were limited in term of amplitude and self sustained, suggesting that energy was being transferred from the moving fluid into the mechanical system. At airspeeds lower than the LCO onset airspeed, the mechanical system loses energy, both to the fluid and to internal damping. At airspeeds higher than the LCO onset condition, the mechanical system absorbs energy from the fluid, such that it can undergo oscillations with limited amplitude.

3.4 Effect of Weakening Structure

There were some cases observed in this work where the leaf springs tested were weakening during oscillations. The weakening was due to crack developed and propagated across the leaf springs as the wing underwent LCOs. Figure 3.4 shows the frequency content for weakening leaf spring occurred for two cases. For case B1, the plate used for the leaf spring was doubled in thickness to amplify the stiffness level.

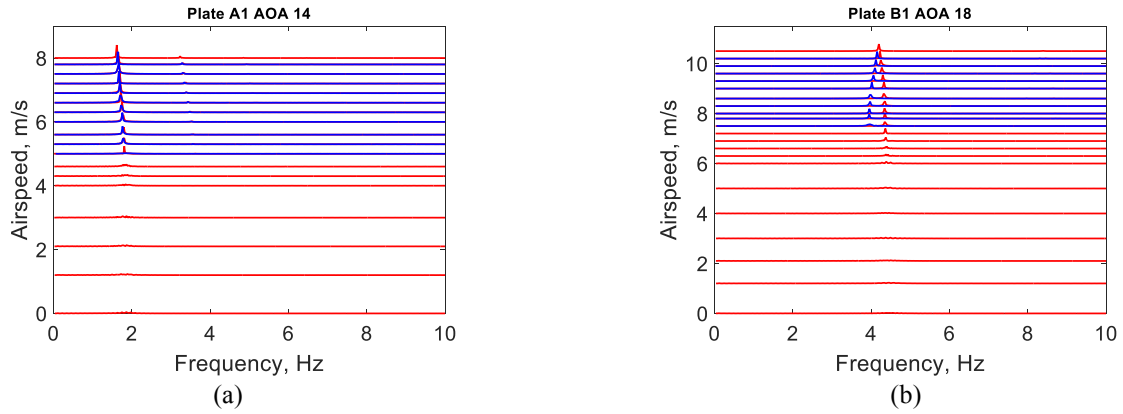

Figure 3.4 : Frequency content for crack leaf spring, (a) plate A1 at 14°, (b) plate B1 at 18°.

From Figure 3.4(a), the frequency decreases as the airspeed increases. The LCOs appear at 5.0 m/s at 1.7Hz. At maximum airspeed of 8.0 m/s, the frequency decreased to 1.5Hz. This indicated that the stiffness was softening. Later investigation revealed that a hairline crack had developed on the leaf spring. Figure 3.4(b) shows a different kind of softening had occurred. LCOs appeared at 6.3 m/s at frequency of 4.3Hz. The frequency decreased as the airspeed was increasing until the maximum speed at 10.5 m/s where the frequency was 4.1Hz. Reducing the airspeed did not increase the frequency as observed in figure 3.4(a) but instead the frequency keep decreasing. The LCOs decayed at 7.5 m/s where the frequency was measured to be 3.8 Hz. Further study to explain this behaviour revealed that the leaf spring also crack. This time the crack was deeper and longer than in the previous case. The size of the crack had altered the structural stiffness of the B1 plate permanently through fatigue failure. Repeating the experiment revealed similar outcome.

3.5 Pressure Distribution

In stall flutter, unsteady static pressure also around the wing was also of interest. Unsteady static pressure can reveal interesting dynamic stall phenomena where the wing experiences a sudden increase in lift before undergoing flow separation and stall. Figure 3.5 presents a snapshot of the pressure distribution around the wing for case A2 oscillating around 12° of static angle of attack at airspeed of 7.2 m/s. The lower surface has higher pressure compared to the upper surface. Figure 3.5(a) shows the pressure distribution plotted with time and chord length for lower surface. The leading edge region experienced alternate pressure condition compared to the rest of the wing. This occurred due to high angle of pitching where the leading edge area experience high suction. High value of negative Cp also indicated that dynamic stall also occurred on the lower side of the wing. This is corroborated by the bifurcation plot where the pitch down angle was also higher that the static stall angle for NACA 0018.

It can be observed that the pressure coefficient at the leading edge on the upper surface, become very negative. Flow separation occurs on the upper surface only while the flow over lower surface remains attached. Such low unsteady pressure coefficient values can be caused by a vortex shedding at the leading edge of the wing. This vortex immediately detaches itself from the surface and propagates downstream. As the wing was pitching down, the flow reattached and pressure recovers on the wing. This process was repeated in every cycle with but varied slightly.

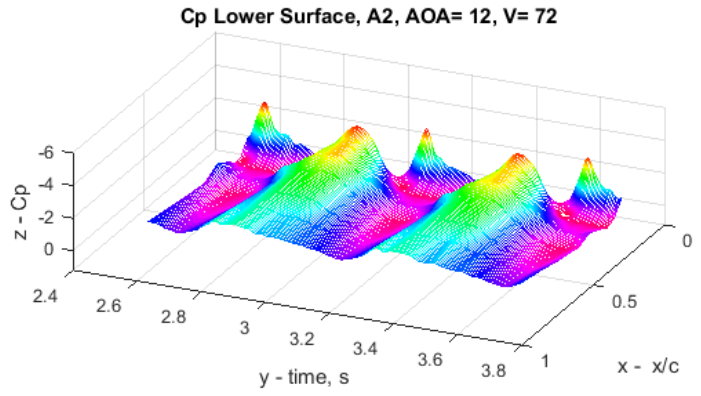

(a)

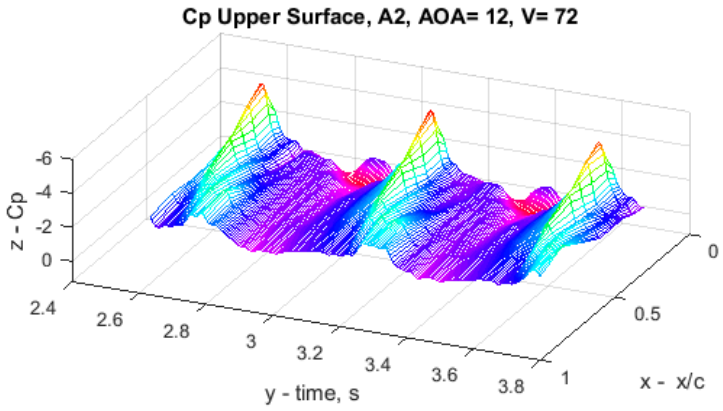

(b)

Figure 3.5 : Pressure distribution around the wing for case A2 at 12° tested at 7.2 m/s for (a) Lower surface, (b) Upper surface.

4 NUMERICAL SIMULATIONS

4.1 Computational setup

In this work, the simulation part was employed to replicate the results observed from the experiement. Only limited cases were simulated due the cost of simulation time was very high. Each case took 20 to 30 days to complete. The flow solver employed was a commercial package of ANSYS FLUENT version 16.1. The flow solver was coupled with the elastically mounted rigid airfoil through user defined function module. Spatial and temporal

discretization were performed with second order schemes for all quantities. The velocity pressure coupling is based on the PISO segregated algorithm for better accuracy. The 2D RANS (SST) $k-\omega$ was used in this work to capture more robust additional flows around the airfoil domain. The time step size utilized for the RANS calculation was $\Delta t = 0.0001$ and the iteration were set up to 500 per time steps. For a stable computations, the time step size was found to be less than 0.001. At each time step, iteration were carried out until a root mean square (RMS) convergence criterion of 10^{-5} on all residuals was reached.

4.2 Mesh and Boundary Conditions

Unstructured meshes were used in the flow domain with inflation-structured meshes at the airfoil boundary layer in this simulation process. The two dimensional pitch-oscillating airfoil was solved in the frame of reference which does not required mesh deformation and re-meshing at the boundary layer in order to obtain better accuracy of the calculations. A circular, non-conformal sliding interface which center located at the elastic axis was used, which only the inner part rotates rigidly along with airfoil while the outer domain remain stationary. Thus, no mesh deformation was required. Periodic boundary condition was applied at the interfaces which allow the flows to enter the rotating domain. Also, this method had been validated in the previous studies [12].

Figure 4.1 shows the computational setup for fluid domain and the rigid airfoil. The rotating domain were set 10c from the point of elastic axis and the static domain were set big enough about 50c to avoid reversed flow error in the fluent software. This reversed flow error happened were caused by the domain as it too small for the fluid to flow. Constant and uniform velocity is imposed at the inlet while constant static pressure is imposed at the outlet. The upper and lower static domain were set symmetry boundary condition, the interior were set automatically by fluent as fluid domain. The first distance from the boundary layer were set based on the Y plus value equal to one.

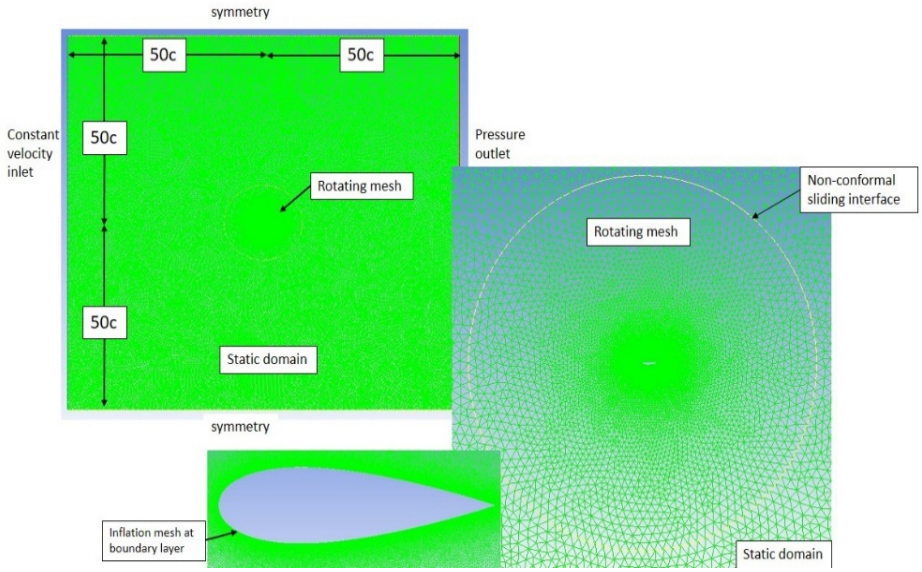

Figure 4.1: Computational domain and grid details.

4.3 Aeroelsatic Modelling

Pitching motion, a one-degree of freedom in pitch mounted rigid body airfoil was modelled based on the equation of motion for aeroelastic system:

$$I_{EA}\ddot{\theta} + D\dot{\theta} + K\theta = M_{EA} \quad (1)$$

The three structural parameters I_{EA}, D, and K were obtained physically from the free vibration test at zero free stream airspeed. The right hand side represents the aerodynamic moment at the elastic axis acting at 0.4c, where I_{EA} is the mass moment of inertia at the elastic axis. The other two parameters D and K is the structural damping coefficient and structural stiffness respectively.

The equation of motion was then solve using Newmark Beta direct time integration method with Newmark's constants. The Newmark Beta method was used to provide pitch position, pitch rate and pitch acceleration at every time step to update the airfoil and the mesh where

$$\theta_{t+\Delta t} = \hat{R}_{t+\Delta t}/\hat{K} \quad (2)$$

$$\ddot{\theta}_{t+\Delta t} = \left(\frac{1}{\propto \Delta t^2}\right)(\theta_{t+\Delta t} - \theta_t) + \theta_t\left(\frac{1}{\propto \Delta t}\right) + \ddot{\theta}_t\left(\frac{1}{2\alpha} - 1\right) \quad (3)$$

$$\dot{\theta}_{t+\Delta t} = \dot{\theta}_t + \ddot{\theta}_{t+\Delta t}(\beta \Delta t) + \ddot{\theta}_t \Delta t(1 - \beta) \quad (4)$$

From the above equations, $\hat{K}$ is the effective stiffness and $\hat{R}_{t+\Delta t}$ is the effective load at each time steps. The value for newmark constants α and β is 0.25 and 0.5 respectively. This values is based on average acceleration method in Newmark method.

In Fluent it is possible to solve the above equations at each time step via user defined functions (UDF) module. This coupled structural equation of motion with the fluid solver. At each time step, Fluent calculates the unsteady aerodynamic forces around the airfoil when fluid interacted with the rigid body. The moment value was then parsed to UDF module for computing the angular pitch velocity for updating the position of the airfoil at each time step. The steps of the calculation can be visualize as shown in Figure 4.2

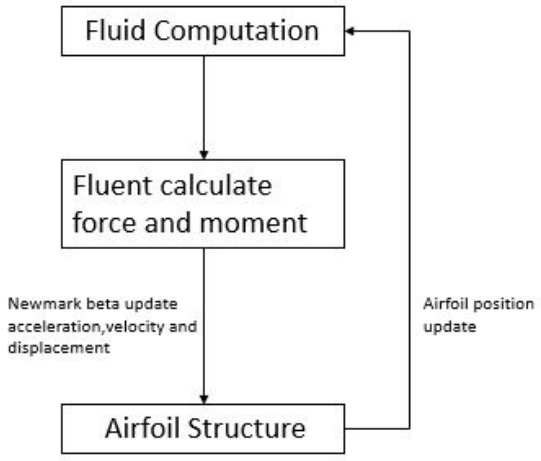

Figure 4.2: Calculation loop.

4.4 Parameter setup

The parameters were obtained physically in the lab and used in the numerical simulation. The mass moment of inertia about the elastic axis was located at 40% of the chord length from the leading edge were $I_\theta = 0.004926\ kgm^2$. The nonlinear structural stiffness equation were obtained from nonlinear stiffness and structural damping were $K_\theta = 1.1706x^3 + 0.3199x^2 + 0.7975x - 0.0029$ and $D_\theta = 0.006934\ Nms/rad$ respectively.

As in the available experimental result, NACA 0018 airfoil was used as the test case. The airfoil had a chord length $c = 0.2\ m$. The simulations were performed at six different airspeeds similar to the wind tunnel freestream airspeeds ranged from 5 m/s to 9 m/s. In the experiment setup, the airfoil was given any initial condition. As for this simulation, the airfoil was also provided with the initial condition of position $\theta = 10$ pitch degrees at the beginning of the simulation and the airflow around the airfoil was initialized with steady flow before the airfoil were released.

4.5 Turbulence Modelling

In this study RANS shear-Stress Transport (SST) $k-\omega$ model is used and this model was develop by Menter [13] to effectively blend the robust and accurate formulation of the standard $k-\omega$ model. It is the combination of a $k-\omega$ model and $k-\varepsilon$ model which produce SST $k-\omega$ that is reliable for a wider class of flows. Also, the Low-Reynolds Correction option activated, this options specifies a low-Reynolds-number correction to the turbulent viscosity and allow for more accurate representation of the actual flow, which was expected to exhibit an attached laminar boundary layer up to separation

5 SIMULATION RESULTS

The computed result are presented and discussed in terms of aeroelastic dynamic responses followed by aerodynamic flow and also comparison between numerical and experimental results.

5.1 Aeroelastic Responses

Figure 5.1 left shows the bifurcation plot for both experiment and simulation observation,as can be seen above both result show the good agreement.The comparison are reasonably good as the simulation resuts produced the similar trend in term of LCO velocity onset and LCO amplitude.The pitch amplitude increases as the free air stream velocity increases.This can observe for both experimental and simulation result. The experimental test were done at limited velocity to avoid damage to the system. Discrepancies between both results can be caused by turbulence modelling as RANS prediction have a tendecncy to overestimate the computed moment. Both agreed that LCO started at $V_\infty = 6\ m/s$ and no LCO phenomena observed at $V_\infty < 6\ m/s$.

Figure 4.3 right shows the comparison LCO pitch frequencies, simulation frequencies increases as the velocity increases but it is vice versa for experiment frequencies as the experiment frequencies decrease with increasing velocity.This behaviour of the experiment frequencies happened is because of the crack on the surface of the airfoil and this has be confirmed by the investigator. At $V_\infty = 0\ m/s$ is the natural frequency of the free vibration

system as no force is applied to the system. LCO frequencies obtained from the computation are quite close to experiment but slightly higher.

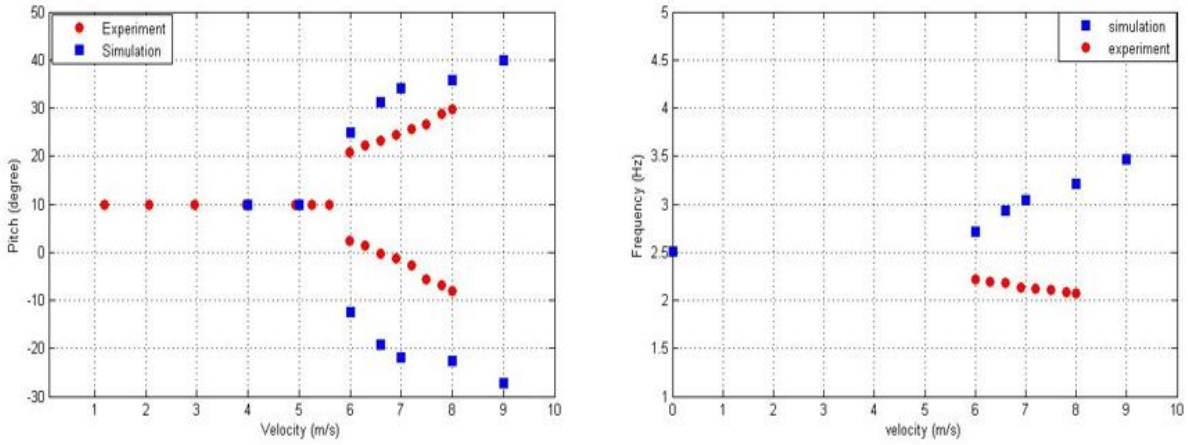

Figure 5.1 : Comparison between experimental and simulation result, left: bifurcation plot and Right: LCO pitch frequency.

Figure 5.2(a) shows the pitch response at the critical LCO velocity when the LCO phenomena started. To recall that the simulation starts with initial condition at $\theta = 10$ pitch degree and the oscillation is sustained throughout the simulation time. The phenomena of deep dynamic

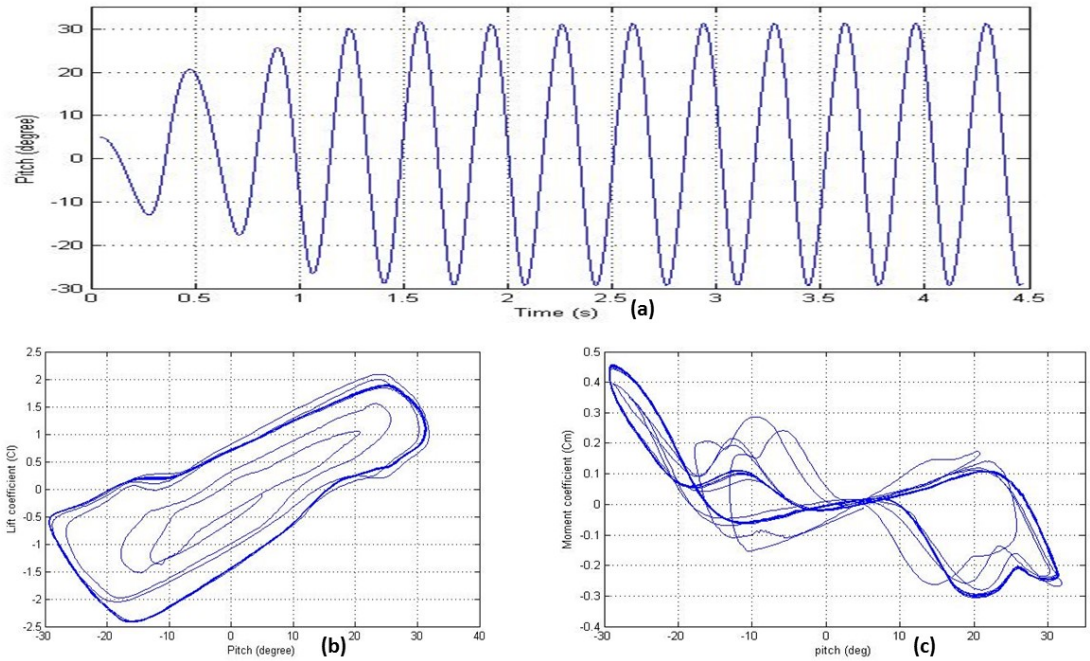

Figure 5.2 : (a) pitch response time history at velocity 6.6 m/s, (b) C_L-pitch plot and (c) C_m-pitch plot .Simulation SST k-ω Rk=6.

stall flutter happened as the pitching angle exceed static flutter angle of attack. Deep stall is heavily influenced by the amount of time the airfoil spends above the steady stall angle and the maximum angle that eventually reaches.

Aerodyanamic damping ζ or the net aerodynamic work per cycle of oscillation is a measure of the net work done by the aerodynamic forces acing on the airfoil. If ζ is negative, the airfoil extracts enegy from the airstream and the picth oscillations will tend to increase in amplitude, while if ζ is positive the fluid receives energy from the airfoil. Stall fluter arising from the negative pitch damping tends to occur when the airfoil is oscillating in and out of stall. As indicate in Figure 5.2(c) the damping is given by the area inside the C_m-pitch trace.

5.1.1 Aerodynamic flow

The location of the flow separation is taken as the point where the wall shear stress equal to zero and the reattachement flow is define when the friction coefficient becomes positive and stay positive. The fluctuations in the wall shear stress profile shows that turbulent vortex manifested on the surface of the airfoil.

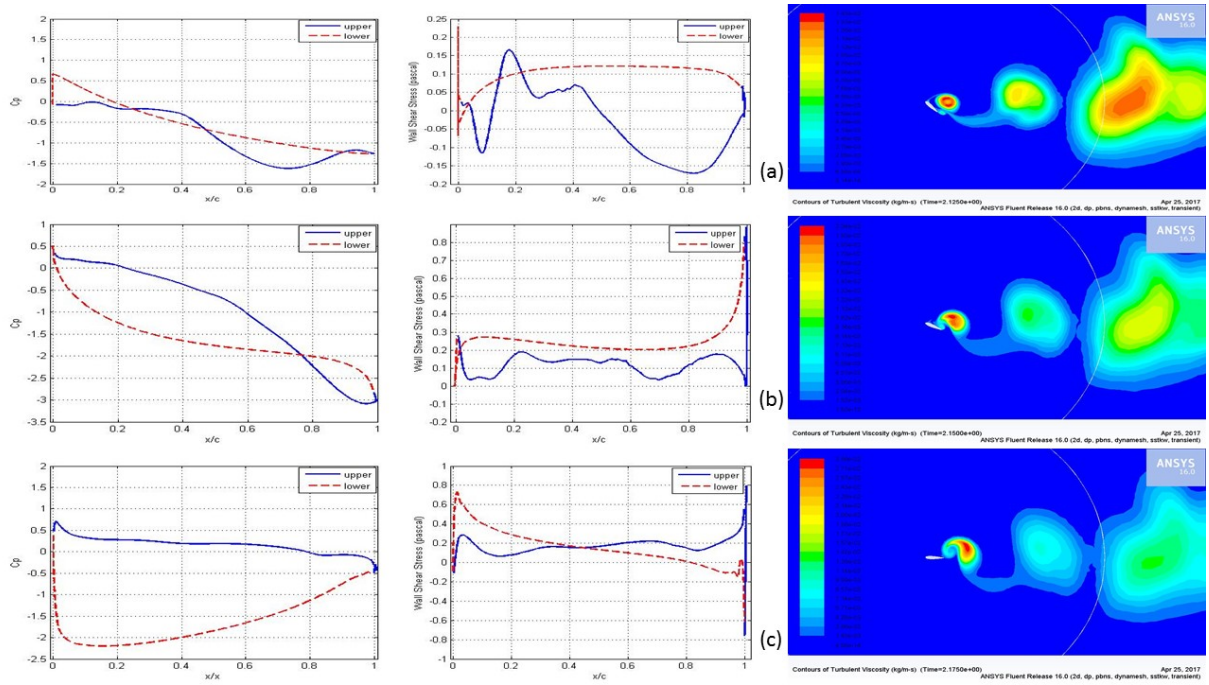

Figure 5.3 : left: Pressure coefficient C_p plot, middle: Wall shear stress plot and right: turbulent viscosity contour.

Figure 5.3 shows the turbulent viscosity contours for dynamic stall pitching airfoil, at (a) as can be seen the airfoil has exceed the static stall angle, there is flow separation from the leading edge transition to trailing edge followed by the formation of 'spilled' vortex. Dynamic stall process involves flow separation and the formation of the vortex disturbance that is cast off from the leading edge region of the airfoil. This vortex disturbance provides additional lift on the airfoil so long as it stays over the upper surface can be seen in (b). These, often surprisingly large increments in lift and are also accompanied by significant increase in nose-down pitching moment, which results from aft moving center of pressure as the vortex disturbance is swept downstream across the chord as can be seen in (c). The sudden break in the lift coefficient occur at a higher angle of attack, moment stall occur at the onset of vortex shedding, where else the lift stall occurs when the vortex passes into the wake. After the vortex disturbance passes the trailing edge of the airfoil and become entrained into the

turbulent wake downstream of the airfoil, the flow on the upper surface progresses to a state of full separation. After the full separation occurred, there is a sudden loss of lift, a peak in the pressure drag and a maximum in nose-down pitching moment. Flow reattachment can take place if and when the angle of attack of the airfoil becomes low enough again.

From the pressure coefficient, the highest pressure were observed at lower surface of the airfoil compared to the upper surface this can be seen from (a) to (c) when the airfoil about to reach the maximum amplitude. The pressure at the lower surface lift the airfoil up ward until it reaches the maximum amplitude. The pressure distribution at the lower surface start to decreases at the trailing edge (c) as the airfoil starts to pitch down. From the observation, high pressure starts to develop at the upper surface caused the airfoil pitching down.

6 CONCLUSION

The bifurcation behavior of a pitching wing with a NACA 0018 section subjected to various static angles of attack and airspeeds was studied. Stall flutter was observed for all chosen angles of attack and stiffness cases. Tests at lower static angle of attack (10°, 12° and 14°) lead higher onset LCO airspeeds, with the LCO amplitudes growing explosively. At higher angles of attack, the lower LCO onset condition was followed by a gradual increase of LCO amplitude as airspeed increases. There was indication of frequency changes with increasing airspeed or variation of the static angle of attack due to the effect of weakening structure. Flow separation occurs on the upper and surface. From the pressure data, flow separation appears at the trailing edge and propagates upstream. In all cases, high-amplitude LCO appears to involve a leading edge vortex generated at the leading edge and subsequently propagating downstream, away from the surface of the wing increasing lift around the wing.

Numerical solutions were performed for NACA 0018 pitch oscillations using RANS (SST) $k-\omega$ model. The predicted LCO onset shows good similarity with the experimental results. However, the simulations were unable to capture the LCOs amplitude measured in the experimental work. Discrepancies between the results can be caused by turbulence modelling as RANS prediction has a tendency to overestimate the lift. The simulation shows that the default Rk value of 6 be able to produce results that have a close agreement with the experimental observation. Coulomb damping could also be the source of discrepancy.

7 ACKNOWLEDGEMENT

This work is supported in part by Universiti Sains Malaysia RU grant 1001/PAERO/814238. The authors would like to thank, Nor Ridwan and M. Isa in School of Aerospace Engineering, Universiti Sains malaysia for their assistance in the experiments.

8 REFERENCES

[1] Halfman, R. L., Johnson, H. C. and Haley, S. M. (1951). *Evaluation of high Angle of Attack Aerodynamic Derivative Data and Stall Flutter Prediction Techniques*. TN-2533, NACA.

[2] Rainey, A. G. (1956). *Preliminary Study of Some Factors which Affect Stall Flutter Characteristic of Thin Wing*. TN-3622, NACA.

[3] Ham, N. D. and Young, M. I. (1966). Limit Cycle Torsional Motion of Helicopter Blades due to Stall. *Journal of Sound and Vibration*, 4(3), 433–444.

[4] Dimitriadis, G. and Li, J. (2009). Bifurcation Behavior of Airfoil Undergoing Stall Flutter Oscillation in Low Speed Wind Tunnel. *AIAA Journal*, 47(11), 2577–2596.

[5] Kuo, C. H. and Hsieh, J. K. (2001). Unsteady low Structure and Vorticity Convection over the Airfoil Oscillationg at High Reduced Frequency. *Experimental and Thermal Fluid Science*, 24(3), 117–129.

[6] Dowell, E. H. (2004). *A Modern Course in Aeroelasticity*. Boston: Kluwer Academic Publisher.

[7] McAlister, K. W., Carr, L. W. and McCroskey, W. J. (1981). Dynamic Stall Experiments on the NACA 0012 Airfoil. TP-1100, NASA.

[8] McCroskey, W. J., McAlister K. W., Carr, L. W., Pucci, S. L., Lambert, O. and Indergrand, R. F. (1981). Dynamic Stall on Advanced Airfoil Sections. *Journal of Americal Helicopter Society,* 26(3), 40-50.

[9] Razak, N. A., Andrrianne, T. and Dimitriadis, G. (2011). Flutter and Stall Flutter of a Rectangular Wing in a Wind Tunnel. *AIAA Journal*, 49(10), 2258-2271.

[10] D. Poirel, V. Métivier, and G. Dumas, "Computational aeroelastic simulations of self-sustained pitch oscillations of a NACA0012 at transitional Reynolds numbers," *J. Fluids Struct.*, vol. 27, no. 8, pp. 1262–1277, 2011.

[11] W. Yuan, B. Wang, D. Poirel, and C. Canada, "Numerical Simulations of Self-Sustained Aeroelastic Oscillations At Low Reynolds Numbers," pp. 1–10, 2011.

[12] T. Kinsey and G. Dumas, "Parametric Study of an Oscillating Airfoil in a Power-Extraction Regime," *AIAA J.*, vol. 46, no. 6, pp. 1318–1330, 2008.

[13] F. R. Menter, "Two-equation eddy-viscosity turbulence models for engineering applications," *AIAA Journal,* vol. 32, pp. 1598-1605, 1994/08/01 1994.

COPYRIGHT STATEMENT